

## The flow of red blood cells through a narrow spleen-like slit

Jonathan B. Freund

Citation: *Phys. Fluids* **25**, 110807 (2013); doi: 10.1063/1.4819341

View online: <http://dx.doi.org/10.1063/1.4819341>

View Table of Contents: <http://pof.aip.org/resource/1/PHFLE6/v25/i11>

Published by the AIP Publishing LLC.

---

### Additional information on Phys. Fluids

Journal Homepage: <http://pof.aip.org/>

Journal Information: [http://pof.aip.org/about/about\\_the\\_journal](http://pof.aip.org/about/about_the_journal)

Top downloads: [http://pof.aip.org/features/most\\_downloaded](http://pof.aip.org/features/most_downloaded)

Information for Authors: <http://pof.aip.org/authors>

### ADVERTISEMENT



**Running in Circles Looking  
for the Best Science Job?**

Search hundreds of exciting  
new jobs each month!

<http://careers.physicstoday.org/jobs>

physicstodayJOBS



## The flow of red blood cells through a narrow spleen-like slit

Jonathan B. Freund<sup>a)</sup>

*Mechanical Science and Engineering and Aerospace Engineering, University of Illinois at Urbana–Champaign, 1206 West Green Street MC-244, Urbana, Illinois 61801, USA*

(Received 18 December 2012; accepted 12 April 2013; published online 30 August 2013)

Small slits between endothelial cells in the spleen are perhaps the smallest blood passages in the body, and red blood cells must deform significantly to pass through them. These slits have been posited to participate in the removal of senescent blood cells from the circulation, a key function of the spleen. One of the effects of red blood cell aging is an increased cytosol viscosity; relaxation time measurements suggest their interior viscosity can increase by up to a factor of 10 toward the end of their normal 120 day circulating lifetime. We employ a boundary integral model to simulate red blood cells as they deform sufficiently to flow through such a small passage, whether in the spleen or in a microfluidic device. Different flow rates and cytosol viscosities show three distinct behaviors. (1) For sufficiently slow flow, the pressure gradient is insufficient to overcome elastic resistance and the cell becomes jammed. (2) For faster flow, the cell passes the slit, though more slowly for higher cytosol viscosity. This can be hypothesized to facilitate recognition of senescent cells. (3) A surprising behavior is observed for high elastic capillary numbers, due either to high velocity or high cytosol viscosity. In this case, the cells infold within the slit, with a finger of low-viscosity plasma pushing deeply into the cell from its upstream side. Such infolding might provide an additional mechanism for jamming, and the sharpness of the resulting features would be expected to promote cell degradation. Linear analysis of a model system shows a similar instability, which is analyzed in regard to the cell flow. This linear analysis also suggests a similar instability for unphysiologically low cytosol viscosity. Simulations confirm that a similar infolding also occurs in this case, which intriguingly suggests that normal cytosol viscosities are in a range that is protective against such deformations. © 2013 AIP Publishing LLC. [<http://dx.doi.org/10.1063/1.4819341>]

### I. INTRODUCTION

Flowing red blood cells are well-known to display complex phenomenology, which is particularly pronounced in geometries of scale comparable to their size.<sup>1,2</sup> In such cases, viscous shear stresses typically overwhelm their relatively weak elastic resistance, leading to complex deformed cell shapes. Thus, red blood cells can quickly flow through passages significantly smaller than their nominal resting shape, a biconcave disk about 8  $\mu\text{m}$  in diameter and 2  $\mu\text{m}$  thick.<sup>1</sup> Since capillary blood vessels are as small as 4  $\mu\text{m}$ ,<sup>3</sup> significant deformations are essential for normal blood perfusion. Disease states such as malaria infection or sickle-cell disease that disrupt the flexibility of red blood cells can cause serious complications.<sup>4</sup> It is now also possible to manufacture devices of the same scale as blood cells, which offers the possibility of testing or sorting blood cells based upon their physical characteristics.<sup>5,6</sup>

We consider the passage of a blood cell through a particularly narrow geometry motivated by the human spleen, which seems to have the smallest blood passages in the human body. Small slits, typically less than 1  $\mu\text{m}$  wide, allow blood cells to pass from the splenic red pulp into the venous

---

<sup>a)</sup>[jbfreund@illinois.edu](mailto:jbfreund@illinois.edu)

system.<sup>6–10</sup> Their resistance to cell passage has been associated with the concentration of red blood cells in the red pulp.<sup>10,11</sup> They have also been shown to be capture points for heat-treated red blood cells.<sup>12</sup> Heat treatment is thought to oxidize hemoglobin and lead to formation of relatively rigid Heinz bodies in the otherwise fluid cytosol within the cells.<sup>13</sup> When small, these particles would increase the effective viscosity of the cytosol, and if they grow large would exceed the size of the splenic slits, presumably causing the cells to be trapped. A similar mechanism involving stiff-body inclusions has also been seen in malaria.<sup>10,14</sup> It seems that the stiffer parasite causes the red blood cells to become either trapped or slowed at the splenic slits, where they are phagocytosized by macrophages or the parasite (along with some membrane and hemoglobin) is “pitted” from the cell, apparently by mechanical rupture.<sup>14</sup> The relative stiffness of the malaria parasite is thought to be a key factor in this. The overall mechanical properties of infected cells<sup>15</sup> are also consistent with the observed impeded flow through small passages.<sup>14</sup>

The slits have also been suggested to play a role in the removal of aged red blood cells.<sup>16</sup> Radiological labeling shows that normal human red blood cells circulate for about 120 days<sup>17,18</sup> before they are removed, largely by the spleen, which somehow targets a relatively narrow distribution of cells near this age. This is supported indirectly by corresponding experiments in mice, which do not have slits in their splenic sinuses<sup>10</sup> and in contrast show a relatively continuous removal across cell ages.<sup>18</sup> This is consistent with a trapping of aged cells by the slits, though there are, of course, other biomechanical and biochemical mechanics that could lead to this same result.

Over their lifetime, red blood cells undergo several changes that might trigger their removal, ultimately by phagocytosis,<sup>7</sup> in the spleen. Observations of the thermal “flicker” on the surfaces of cells show that the motions become simpler with age, closer to that of strictly Brownian motion, indicating a decreased role of the membrane structural properties relative to the viscous properties of the overall system.<sup>19</sup> The success of frequency independent fits of flicker-based correlations with a model that excludes membrane viscosity indicates that cytosol viscosity dominates their dissipation.<sup>20</sup> An increased cytosol viscosity has been suggested to be the dominant age-related mechanical change that suppresses cell deformation in response to shear.<sup>21–23</sup> Based upon measurements of bulk hemoglobin,<sup>24,25</sup> the observed concentration of the cytosol is anticipated to increase its viscosity by a factor of around 5 with age; Williams and Morris<sup>26</sup> anticipate an increase from 0.009 to 0.054 Pa s, which corresponds to a viscosity ratio  $\lambda = \mu_{\text{cytosol}}/\mu_{\text{plasma}}$  that increases from  $\lambda \approx 7.5$  to  $\lambda \approx 45$ . Increased acoustic attenuation by aged red blood cells also supports an increased hemoglobin concentration and cytosol viscosity.<sup>27</sup> Direct measurements of the relaxation of cellular deformation show that older cells relax more slowly,<sup>28</sup> with a few aged cells relaxing at only one-tenth the rate of the mean.<sup>29</sup> We focus on cytosol viscosity, neglecting membrane viscosity, because the large change in viscosity seems to be associated primarily with the cytosol. Only if membrane viscosity is deduced inversely from observed relaxation times, *a priori* neglecting cytosol viscosity, is it deemed to be dominant.<sup>28</sup> There is also relatively little change observed in the elastic modulus of the cells with age.<sup>28,30</sup>

It has been suggested that the increased cytosol viscosity might be a key trigger for removal in the spleen.<sup>26</sup> To explore the mechanical aspects of this, we consider a model of red blood cells passing through a spleen-like slit, which is introduced in detail in Sec. II. Since their precise properties are not accurately measured and vary from slit-to-slit, we have designed it to represent in detail only its main features: a 1  $\mu\text{m}$  wide gap between rounded walls. Though motivated by the spleen, the more important implications of this work might be in manufactured devices, designed either to replicate spleen-like functions or with other objectives. The details of the numerical model used to simulate the passage of red blood cells through the slit are presented in Sec. III.

The full mechanisms of identification of relatively aged cells certainly involves complex biochemistry. However, given that the mechanical changes that occur with aging are so pronounced, we focus on how these affect passage of the slits and might trigger whatever capture occurs. Though we can speculate that aged cells become fragile, it would be surprising if the sequestration of aged cells were based upon a simple “stress test,” since stressing to near breaking in general accelerates degradation. It is known that cells processed mechanically can experience subhemolytic trauma,<sup>1</sup> which is expected to be small for physiologically normal conditions. We therefore are particularly interested in any changes in the fundamental flow behavior that occur along with the physiological

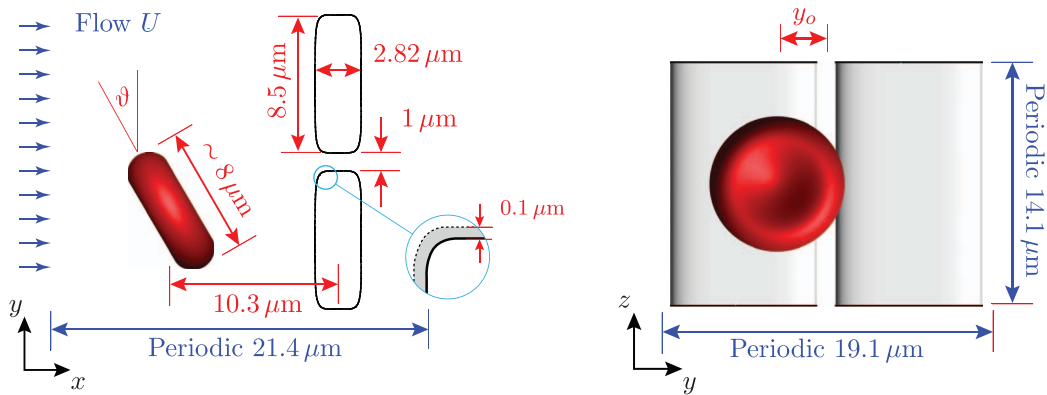


FIG. 1. Slit-flow initial condition.

changes associated with cell aging. A jamming at low flow rates and an apparent bifurcation to an infolding behavior are both observed and presented in Sec. IV. The character of the unexpected infolding behavior is consistent with the results of a closed-form analysis of a linear model presented in Sec. V.

## II. MODEL CONFIGURATION

The model slit geometry is shown in Figure 1. Two cylindrical rigid boundaries of shape

$$x = \pm \frac{a_o}{2} (\cos \theta)^{\frac{1}{3}}, \quad y = \pm \frac{3a_o}{2} (\sin \theta)^{\frac{1}{3}}, \quad \text{for } \theta \in [0, \pi/2), \quad (1)$$

are positioned to form a slit that is  $1 \mu\text{m}$  wide and  $2.82 \mu\text{m}$  long. Here,  $a_o = 2.82 \mu\text{m}$  is the radius of a sphere matching the volume of a red blood cell. The cell is initialized in its biconcave reference shape as shown, with its centroid  $10.3 \mu\text{m}$  upstream of the slit, inclined at angle  $\vartheta$  and offset by  $y_o$ . The domain is triply periodic as labeled, with the red blood cell flowing through one of the two such slits included in the domain.

A constant mean flow  $U$  pushes the cell through the slits in the  $x$ -direction. Because of the coupled character of viscous flow, it cannot be assumed *a priori* that either a splenic slit or a microfluidic device of similar geometry would operate at an exactly constant pressure or constant flow rate condition. A fixed flow rate is assumed for convenience and it should be noted that pressure gradients typically increase by about 30% as the cells pass through the slit. For relatively low internal viscosity ( $\lambda = 5$ ) and the highest flow rates considered, this pressure increase drops to 20%.

Endothelial cells in the microcirculation are lined with a layer of glycoproteins and related molecules—the endothelial glycocalyx.<sup>31</sup> For flowing red blood cells in small vessels, the hydrodynamic influence of this layer suggests that it is  $0.5 \mu\text{m}$  thick, however stiffer white blood cells in small vessels appear to crush the layer down to around  $0.1 \mu\text{m}$ .<sup>31</sup> Although its thickness does not appear to have been measured in the spleen, it is assumed that the endothelial cells that make up the slits are similarly lined. Since the red blood cells flow slowly through it and are particularly confined, they are assumed to crush the glycocalyx more than they do in capillaries. This layer is thus modeled simply as an exclusion zone of thickness  $0.04a_o = 113 \text{ nm}$  (see Figure 1). Cell membranes are simply moved outside this distance in the direction of the surface normal at the end of each discrete time step when they approach more closely than this.<sup>34</sup> Though this obviously does not represent all the sub-micrometer mechanics of the glycocalyx, a more realistic model is beyond the scope of the present study, especially given the scant experimental data available upon which to base it.

The red blood cell membrane is modeled as an elastic shell using the two-parameter constitutive model of Skalak,<sup>32</sup> which is crafted in terms of invariants

$$I_1 = \lambda_1^2 + \lambda_2^2 - 2 \quad \text{and} \quad I_2 = \lambda_1^2 \lambda_2^2 - 1, \quad (2)$$

where  $\lambda_1$  and  $\lambda_2$  are the principal in-plane stretches. (These invariants correspond to the the first and third invariants of the left Cauchy–Green tensor for  $\lambda_3 = 1$ .) With these, he postulated a strain energy

$$W = \frac{E_S}{4} \left( \frac{1}{2} I_1^2 + I_1 - I_2 \right) + \frac{E_D}{8} I_2^2, \quad (3)$$

which affords independent specification of weak resistance to in-plane shear via  $E_S$  and strong resistance to area dilatation via  $E_D$ , as observed for red blood cells. The specific parameters used match those of Pozrikidis,<sup>33</sup> which are based upon experimental measurements: shear modulus  $E_S = 4.2 \times 10^{-6}$  N/m and  $E_D = 67.7 \times 10^{-6}$  N/m. A resistance to bending deformations is likewise represented with modulus  $E_B = 1.8 \times 10^{-19}$  N m as described elsewhere.<sup>34</sup> Although such a simple model is incapable of representing with high fidelity all the potential deformations a red blood cell might experience, it is employed because it is well-defined and widely used and represents the key features of red blood cell dynamics. It has been used to match the effective viscosity measurements for round tubes ranging in diameter from  $D = 5 \mu\text{m}$  up to  $D = 28 \mu\text{m}$ .<sup>34,35</sup>

The blood plasma has viscosity  $\mu_p = 0.0012$  Pa s and the Newtonian<sup>24</sup> hemoglobin solution that constitutes the cytosol of the red blood cell has viscosity  $\mu_c = \lambda\mu_p$ , with  $\lambda = 5$  often considered physically normal for an average red blood cell.<sup>33</sup> For clarity,  $U_o = 282 \mu\text{m/s}$  is taken as a velocity scale, consistent with the nondimensionalization employed in developing and validating the simulation model,<sup>34</sup> but dimensional results are also provided in many places given that it is the unique properties of the red blood cells that motivate this study.

### III. FLOW SOLVER

The Reynolds number based upon the largest at rest cell dimension of  $8 \mu\text{m}$ , a fast flow rate of  $1 \text{ mm/s}$ , and the plasma viscosity  $\mu_p$  is  $Re < 0.01$ , which justifies approximating the flow equations by their viscous limit and enables their formulation into boundary integrals.<sup>36,37</sup> Our fast solver for the resulting system was reported elsewhere<sup>34,35</sup> and has been used in recent studies of flow in small tubes<sup>38</sup> and the transport of nanometer-scale magnetic beads.<sup>39</sup> A key feature of the algorithm is the spectral representation of the cell shapes with spherical harmonics, which both affords excellent resolution and facilitates a dealising procedure that obviates the need for any artificial dissipation or filtering, either of which would degrade the resolution. For the simulations reported herein, spherical harmonics of maximum degree  $N = 32$  were employed, which corresponds to  $N^2$  degrees of freedom per coordinate direction. Nonlinear expressions were calculated with a  $M = 3N$  maximum degree representation. A detailed resolution and convergence study for a similar geometry is reported elsewhere.<sup>34</sup>

Each of the solid walls is represented by 9696 triangular elements. These are uniformly distributed on a unit circle with  $\phi \in [0, 2\pi)$  and mapped such that  $\theta = \phi - 0.25\sin 4\phi$  in (1). The result is a three times denser element spacing in the slit than on the lateral sides.

### IV. SIMULATION RESULTS

For  $U = 0.125U_o \equiv U_1 = 35 \mu\text{m/s}$ , the cell slowly passes through the slit, but for slower flow the elastic resistance of the cells stops it as visualized in Figure 2. These cases were simulated with  $\lambda = 20$ , but the results are  $\lambda$ -independent for these cases in which the cell becomes jammed. For  $U = U_1/2$ , the cell enters the slit and protrudes slightly out the far side, but then stops. For still slower velocities, it protrudes less and less into the slit. All these jammed-cell simulations were run until the cell centroid velocity was steadily below  $5 \times 10^{-5}U_o \approx 10 \text{ nm/s}$  and still decelerating. We thus conclude that for the current model the cell would never pass, though actual red blood cells might display a more complex behavior. For example, some cells that have been observed to pass through splenic slits over tens of seconds,<sup>11</sup> which correspond to the time over which the cytoskeleton is expected to remodel.<sup>40</sup>

For  $U \geq 0.125U_o$ , the cells pass through the slit, as shown for a particular case in Figure 3 (enhanced online). The transit time depends strongly upon the cell-interior viscosity (Figure 4),

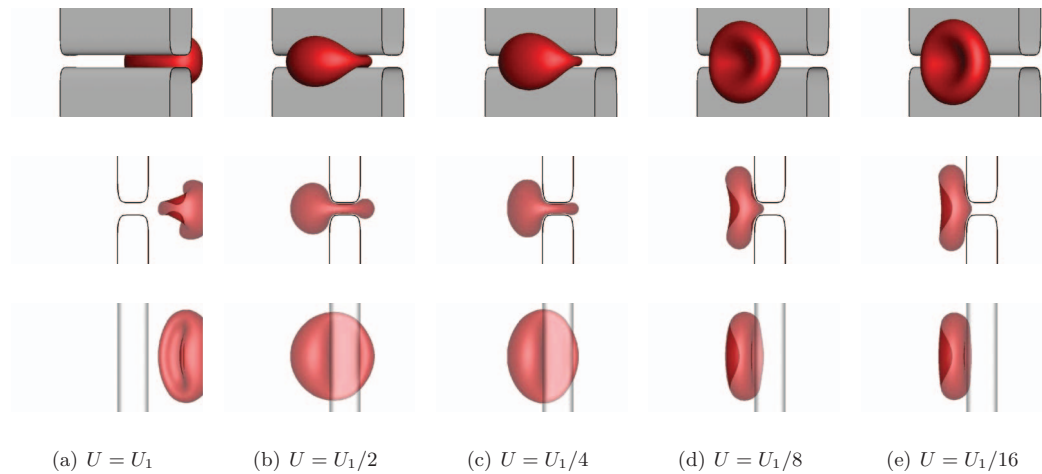


FIG. 2. (a) For  $U = U_1 = 0.125U_o = 35 \mu\text{m/s}$ , the cell passes, but at the times shown velocities have dropped to near zero for (b) through (e). Note that given the relatively low deformation of the membrane in these cases, the maximum spherical harmonic degree was decreased to  $N = 24$ .

indicating that a significant fraction of the viscous dissipation arises within the cell. However, it should be clear that in all cases the red blood cell does indeed pass through the slit, with the increased viscosity only slowing it. This delay might facilitate phagocytosis by monocytes, but despite slowing due to increased viscosity, passage is still faster than the anticipated crawling velocities of monocytes.

While elastic jamming and viscosity mediated transit are qualitatively as might be anticipated, still larger  $\lambda$  or  $U$  leads to a third, more surprising behavior. An example of this is visualized in Figure 5 (enhanced online). The cell begins to pass through the slit, as in the case visualized in Figure 3. However, instead of deforming into a dumbbell-like shape once it is fully within the slit, a finger of relatively low-viscosity plasma deforms the cell membrane on its trailing side, leading to an infolding of the cell. This behavior is reminiscent of viscous fingering in that the low viscosity fluid—here the plasma—is more easily drawn toward the slit than the higher viscosity cytosol.

The cases that show the infolding are obviously at risk to become under-resolved in the neighborhood of the sharp cusp-like leading edge of the penetrating low-viscosity fluid. Were these

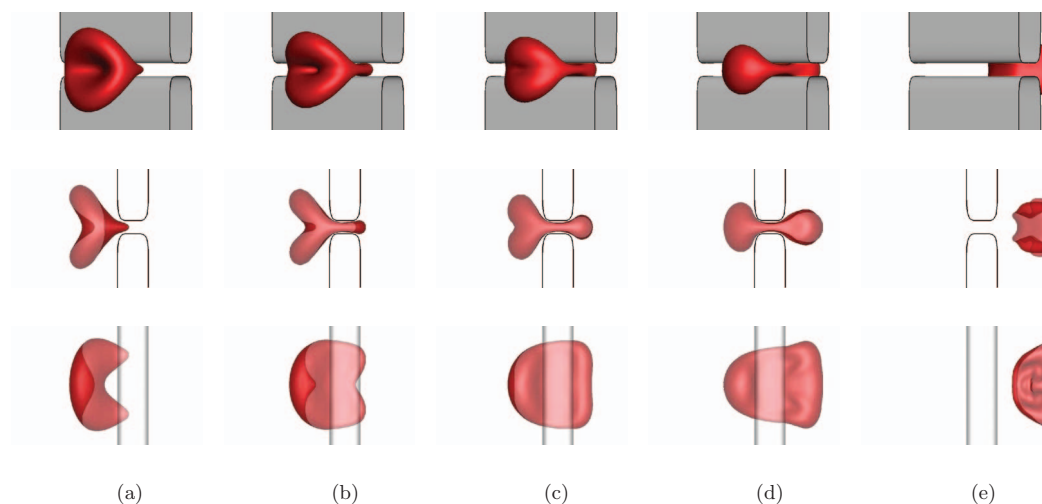
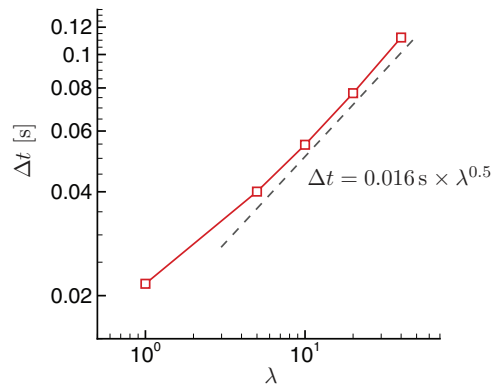
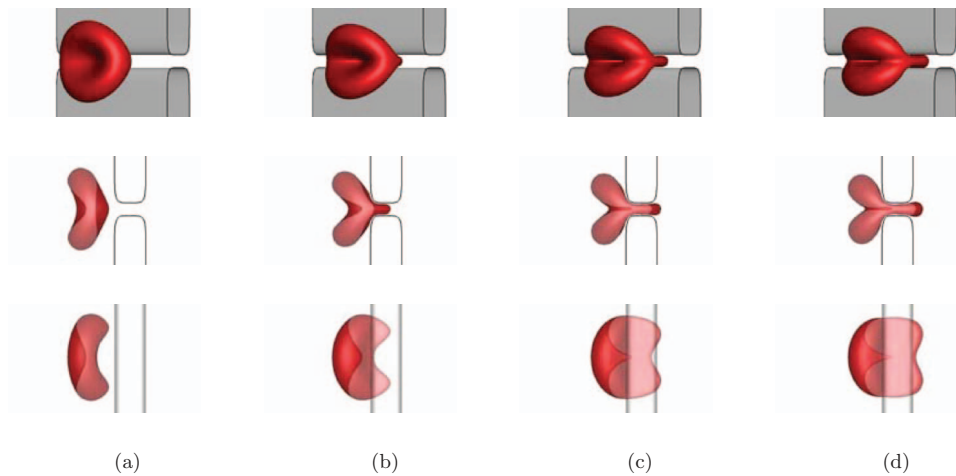
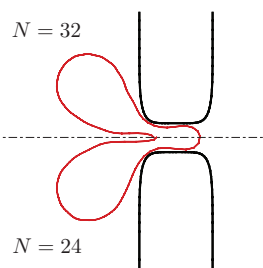


FIG. 3. (a)  $t = 10 \text{ ms}$ , (b)  $t = 11.25 \text{ ms}$ , (c)  $t = 12.5 \text{ ms}$ , (d)  $t = 15.0 \text{ ms}$ , (e)  $t = 20.0 \text{ ms}$ . Visualization of a cell passing through the slit for  $U = 2.0U_o = 560 \mu\text{m/s}$ ,  $\lambda = 5$  (enhanced online). [URL: <http://dx.doi.org/10.1063/1.4819341.1>]

FIG. 4. Transit time for  $U = 0.5U_o = 141 \mu\text{m/s}$ .FIG. 5. (a)  $t = 10$  ms, (b)  $t = 11.25$  ms, (c)  $t = 12.5$  ms, (d)  $t = 13.25$  ms. Visualization for  $U = 2U_o$ ,  $\lambda = 20$  showing infolding behavior (enhanced online). [URL: <http://dx.doi.org/10.1063/1.4819341.2>]FIG. 6. Resolution comparison at  $t = 11.75 \mu\text{m}$  for the infolding-cell case of Figure 5.

simulations continued, they would soon so exceed the resolution capacity of  $N = 32$  degree spherical harmonics that they would become numerically unstable via some combination of overwhelming the dealising, accessing more numerically stiff deformations via the nonlinear constitutive model, or numerical errors that lead to intersection with other membrane surfaces or walls. However, up to the point we report here, the observations are mesh independent. Figure 6 shows the same time for an infolding simulation with maximum degree  $N = 24$  spherical harmonics, rather than our typical  $N = 32$ . The overall shape is nearly indistinguishable despite the diminished resolution.

The velocity–viscosity parameter space spanning the three behaviors for a physiological range of  $\lambda$  is shown in Figure 7. There is an apparent sharp change in behavior between jamming and

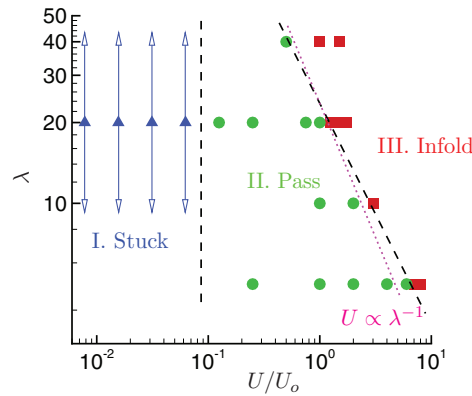


FIG. 7. The three behaviors for various  $U$  and  $\lambda$ :  $\blacktriangle$  stuck;  $\bullet$  pass; and  $\blacksquare$  infold. The - - - lines are hand drawn apparent boundaries. The ..... line corresponds to a capillary number scaling (5).

passing at a critical value of  $U$ . When the cell stops, its interior viscosity is irrelevant so this jamming is independent of  $\lambda$ . The corresponding elastic capillary number based on the plasma viscosity is expectedly low,

$$Ca_p \equiv \frac{\mu_p U}{E_S} = 0.01. \tag{4}$$

Here, we use the shear modulus  $E_S$  rather than the bending modulus  $E_B$  because it is generally more important than the bending resistance, except when sharp folds form. The corresponding capillary number based upon the bending modulus is indeed relatively large:  $Ca_b = \mu_p U a_o^2 / E_B = 1.87$ . In contrast, the switch between the pass-through and infolding behaviors depends upon cytosol viscosity and follows closely a line with  $U \propto \lambda^{-1}$ . This apparent bifurcation is parameterized by an elastic capillary number based upon the cytosol viscosity,

$$Ca_c \equiv \frac{\mu_c U}{E_S} = 1.9, \tag{5}$$

for cases with  $\vartheta = 0$  and  $y_o = 0$  (see Figure 1). Changing  $\vartheta$  or offset  $y_o$  decreases its cross-stream profile as it encounters the slit in a manner that suppresses infolding. However, infolding is not eliminated. Rather, it simply occurs at a larger  $Ca_c$ , as seen in Figure 8.

The dependence of infolding on the elastic capillary number suggests that elasticity resists the infolding behavior whereas viscous stresses promote it. To see this in more detail, in Figures 9(a)

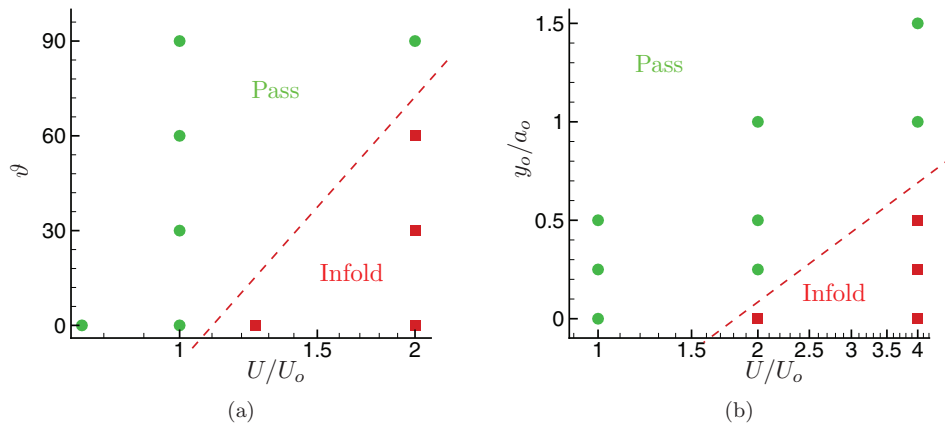


FIG. 8. Behavior for other initial (a) orientation angles  $\vartheta$  and (b) offsets  $y_o$  as defined in Figure 1:  $\bullet$  pass; and  $\blacksquare$  infold. The - - - lines are hand drawn apparent boundaries.

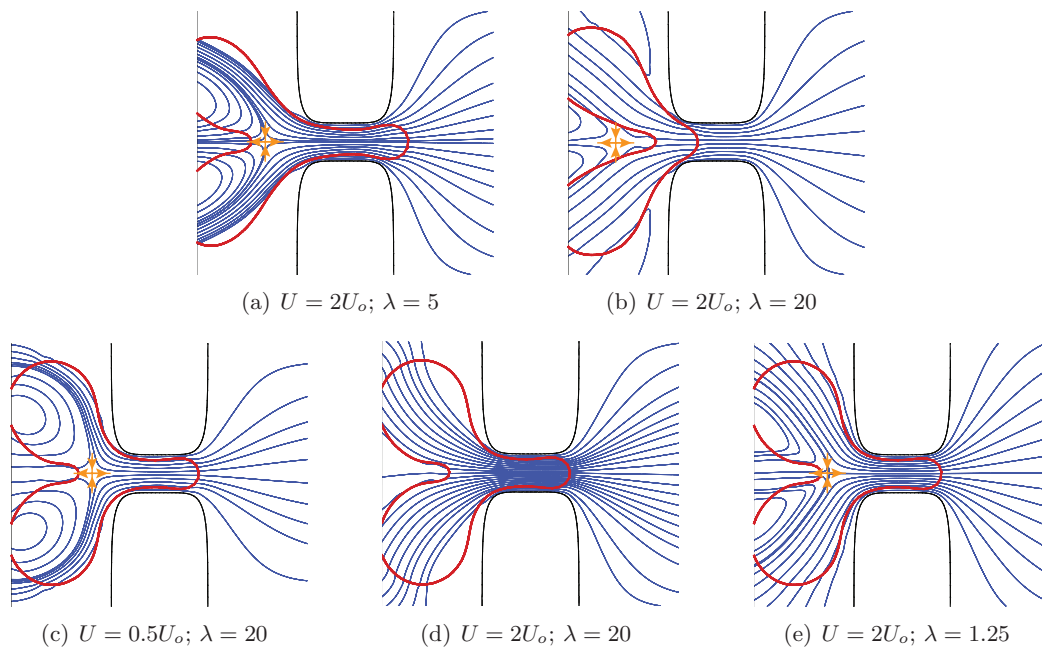


FIG. 9. (a)–(c) Streamlines for cases as labeled; (d)–(e) streamlines after a change from the case in (c) to the new parameters as labeled.

and 9(b) we examine the velocity field for cases near either side of the apparent bifurcation. At a similar time, the lower  $Ca_c$  case shows a stagnation point within the cell, which corresponds to a backflow that pushes the low-viscosity finger out of the cell, countering its tendency to infold. For  $\lambda = 20$  (Figure 9(b)), the stagnation point is in the low-viscosity plasma and will lengthen the finger of low-viscosity fluid. Though this is suggestive, such comparisons at a particular time are hampered because disparate evolution histories have already led to significantly different cell shapes. To mitigate this, we take advantage of the negligible inertia and change  $\lambda$  and  $U$  instantaneously to show their effect for a particular cell shape. Figure 9(c) shows the cell cross-section and streamlines for a case that does not infold. Increasing  $U$  by a factor of 4, which would correspond to infolding case in Figure 7, leads to the flow visualized in Figure 9(d). The stagnation point is no longer inside the cell and it is expected that the less viscous fluid will be more easily drawn into the slit than the cytosol. Running the simulation confirms this is the subsequent progression. In contrast, if  $U$  is increased by the same factor of 4 but  $\lambda$  decreased to  $\lambda = 1.25$ , approximately maintaining the initial low  $Ca_c$ , the stagnation point again returns to the interior of the cell in a way that would counter infolding.

## V. LINEAR ANALYSIS OF A TWO-DIMENSIONAL MODEL SYSTEM

### A. Formulation

The full details of the slit passage, particularly when the cell infolds, obviously involve the coupled viscous flow and finite-deformation elasticity of the cells. However, the basic infolding bifurcation seems to arise from the same simple balance of viscous versus elastic forces expected for the model system shown in Figure 10. A fluid of viscosity  $\mu^-$  is withdrawn at rate  $-Q$  from the center of a round elastic membrane of initial radius  $a_o$ . The sink models the flow into the slit, phenomenologically representing it without the influence of the cell. Only after the cell is significantly deformed does it give rise to the stagnation points seen in Figure 9. Exterior to this membrane is a fluid of viscosity  $\mu^+ = \mu^-/\lambda$ , with  $\lambda$  thus defined as for the cell simulations. We are interested in the growth and decay of perturbations to the membrane shape  $\eta(\theta, t)$ .

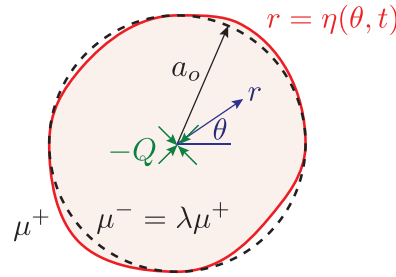


FIG. 10. Point extraction of a viscous fluid bounded by an elastic membrane.

In considering this configuration, we must recognize that it is a linear model designed to share characteristics of the full system. It is obviously not a linearization of the full system, which would be challenging and not necessarily as illuminating as this simpler model. It will show amplification of deformations for some sets of parameters, which we will designate instabilities, though it does not constitute a traditional stability analysis with a well-defined baseflow. It should, instead, be considered a tractable model that includes the key mechanical interactions in the cell flow.

The flow is governed by the Stokes equation, both for  $r > \eta$  and  $r < \eta$ , which are designated the + and - regions, respectively,

$$\nabla p = \mu^\pm \nabla \cdot (\nabla \mathbf{u} + (\nabla \mathbf{u})^T), \quad (6)$$

with the usual incompressibility constraint

$$\nabla \cdot \mathbf{u} = 0. \quad (7)$$

The pressure is  $p$  and cylindrical coordinate velocity components make up  $\mathbf{u}$ ,

$$\mathbf{u} = (v_r, v_\theta) = \left( \frac{1}{r} \frac{\partial \psi}{\partial \theta}, -\frac{\partial \psi}{\partial r} \right), \quad (8)$$

where the streamfunction  $\psi$  leads to the usual biharmonic equation

$$\nabla^4 \psi = 0. \quad (9)$$

The pressure satisfies a Laplace equation

$$\nabla^2 p = 0. \quad (10)$$

The steady perturbation-free baseflow is that of a point source ( $Q > 0$ ) or sink ( $Q < 0$ ),

$$V_r = \frac{Q}{2\pi r}, \quad (11)$$

and is continuous across the membrane. The corresponding baseflow pressure  $P^\pm$  is uniform except for a possible jump at the membrane  $r = \eta(\theta, t)$ , which will be determined by dynamic conditions on the membrane. The full flow solution and membrane shape, denoted symbolically here with a superscript  $t$ , is decomposed into a base solution plus perturbation as

$$v_r^t(r, \theta, t) = V_r(r) + v_r(r, \theta, t), \quad (12)$$

$$v_\theta^t(r, \theta, t) = 0 + v_\theta(r, \theta, t), \quad (13)$$

$$p^t(r, \theta, t) = P(r) + p(r, \theta, t), \quad (14)$$

$$\psi^t(r, \theta, t) = \frac{Q}{2\pi} \theta + \psi(r, \theta, t), \quad (15)$$

$$\eta^t(\theta, t) = \eta(\theta, t) = a_o + a'(t) + \eta'(\theta, t), \quad (16)$$

where  $a_o$  is the initial membrane radius and  $a'(t)$  is the axisymmetric perturbation to it, so  $\eta'$  only includes perturbations that vary in  $\theta$  and time.

## B. Boundary conditions

Velocity perturbations are assumed to decay for  $r \rightarrow \infty$ ,

$$v_r(r \rightarrow \infty) = 0 \quad \text{and} \quad v_\theta(r \rightarrow \infty) = 0, \quad (17)$$

and are bounded at  $r = 0$ . Continuity of velocity is enforced on the membrane

$$v_r(\eta^-) = v_r(\eta^+) \quad \text{and} \quad v_\theta(\eta^-) = v_\theta(\eta^+). \quad (18)$$

Consistent with the negligible inertia of Stokes flow, the membrane itself is assumed to have negligible mass and is thus simply advected by the flow. Taking  $f(r, \theta, t) = \eta(\theta, t) - r$  to designate the interface material, this kinematic condition at  $r = \eta$  leads to

$$\frac{Df}{Dt} = \frac{\partial \eta}{\partial t} - v_r' + \frac{v_\theta}{\eta} \frac{\partial \eta}{\partial \theta} = 0. \quad (19)$$

Applying (11), (12), and (16) yields

$$\frac{\partial a'}{\partial t} + \frac{\partial \eta'}{\partial t} - \frac{Q}{2\pi\eta} - v_r + \frac{v_\theta}{\eta} \frac{\partial \eta'}{\partial \theta} = 0. \quad (20)$$

Linearizing leads to the expected change of the circular radius of membrane due to the baseflow,

$$\frac{\partial a'}{\partial t} = \frac{Q}{2\pi(a_o + a')}, \quad (21)$$

and a condition on the non-axisymmetric membrane perturbations  $\eta'$

$$\frac{\partial \eta'}{\partial t} + \frac{Q}{2\pi a_o^2} \eta' - v_r = 0. \quad (22)$$

The dynamic boundary conditions must account for the elastic resistance of the membrane. We assume that its tension  $\tau$  in response to stretching is

$$\tau = T \left( \frac{ds}{ds_o} - 1 \right), \quad (23)$$

where  $s$  is its arc length with reference length  $s_o$  and  $T$  is an elastic tension modulus, and that its moment  $b$  in response to bending is

$$b = M(\kappa - \kappa_o), \quad (24)$$

where  $\kappa$  is curvature with reference curvature  $\kappa_o$  and  $M$  is an elastic bending modulus. To leading order, the tension and bending moment are

$$\tau = T \frac{\eta'}{a_o} \quad \text{and} \quad b = M \left[ \frac{1}{a_o} \left( 1 - \frac{\eta'}{a_o} - \frac{1}{a_o} \frac{\partial^2 \eta'}{\partial \theta^2} \right) - \kappa_o \right]. \quad (25)$$

A force balance on an infinitesimal membrane segment yields the traction it exerts on the fluid,

$$\Delta \mathbf{F} = \frac{\partial \tau \mathbf{t}}{\partial s} + \frac{\partial}{\partial s} \left( \frac{\partial b}{\partial s} \mathbf{n} \right), \quad (26)$$

where  $\mathbf{t}$  and  $\mathbf{n}$  are, respectively, its counterclockwise ( $+\theta$ ) pointing tangent and outward ( $+r$ ) pointing normal. To leading order,

$$\mathbf{t} = (-\sin \theta, \cos \theta) \equiv \mathbf{e}_\theta \quad \text{and} \quad \mathbf{n} = (\cos \theta, \sin \theta) \equiv \mathbf{e}_r, \quad (27)$$

which upon combination with (25) leads eventually to

$$\Delta \mathbf{F} = - \left[ \frac{T}{a_o^2} \eta' + \frac{M}{a_o^4} \left( \frac{\partial^2 \eta'}{\partial \theta^2} + \frac{\partial^4 \eta'}{\partial \theta^4} \right) \right] \mathbf{e}_r + \left[ \frac{T}{a_o^2} \frac{\partial \eta'}{\partial \theta} - \frac{M}{a_o^4} \left( \frac{\partial \eta'}{\partial \theta} + \frac{\partial^3 \eta'}{\partial \theta^3} \right) \right] \mathbf{e}_\theta. \quad (28)$$

The elastic traction causes a corresponding jump in the fluid stresses at the membrane,

$$\llbracket \boldsymbol{\sigma} \cdot \mathbf{n} \rrbracket = \Delta \mathbf{F}, \quad (29)$$

which constitutes a pair of dynamic boundary conditions for the Newtonian viscous stress  $\boldsymbol{\sigma}$ . The normal component is

$$\llbracket \mathbf{n} \cdot \boldsymbol{\sigma} \cdot \mathbf{n} \rrbracket = \left[ -p^t + 2\mu \frac{\partial v_r^t}{\partial r} \right]_{\eta^-} - \left[ -p^t + 2\mu \frac{\partial v_r^t}{\partial r} \right]_{\eta^+} = \mathbf{n} \cdot \Delta \mathbf{F}. \quad (30)$$

At leading order, this is a jump condition on the axisymmetric baseflow pressure,

$$P(a_o^+) - P(a_o^-) = (\mu^- - \mu^+) \frac{Q}{\pi a_o^2}, \quad (31)$$

and with (28) linearization yields a condition on the perturbations,

$$\left[ -p + 2\mu\eta' \frac{Q}{\pi a_o^3} + 2\mu \frac{\partial v_r'}{\partial r} \right]_{a_o^-} - \left[ -p + 2\mu\eta' \frac{Q}{\pi a_o^3} + 2\mu \frac{\partial v_r'}{\partial r} \right]_{a_o^+} = \frac{T}{a_o^2} \eta' + \frac{M}{a_o^4} \left( \frac{\partial^2 \eta'}{\partial \theta^2} + \frac{\partial^4 \eta'}{\partial \theta^4} \right). \quad (32)$$

By the same procedure, the tangential component  $\llbracket \mathbf{t} \cdot \boldsymbol{\sigma} \cdot \mathbf{n} \rrbracket = \mathbf{t} \cdot \Delta \mathbf{F}$  of (29) leads to a second dynamic condition on the perturbations,

$$\mu^- \left[ \frac{\partial v_\theta}{\partial r} + \frac{1}{r} \frac{\partial v_r'}{\partial \theta} - \frac{v_\theta}{r} \right]_{a_o^-} - \mu^+ \left[ \frac{\partial v_\theta}{\partial r} + \frac{1}{r} \frac{\partial v_r'}{\partial \theta} - \frac{v_\theta}{r} \right]_{a_o^+} = -\frac{T}{a_o^2} \frac{\partial \eta'}{\partial \theta} + \frac{M}{a_o^4} \left( \frac{\partial \eta'}{\partial \theta} + \frac{\partial^3 \eta'}{\partial \theta^3} \right). \quad (33)$$

### C. Solution

The geometry suggests the usual separation-of-variables form for cylindrical coordinates,

$$\psi^\pm(r, \theta, t) = f^\pm(r) e^{im\theta} e^{\alpha t}, \quad (34)$$

$$p^\pm(r, \theta, t) = g^\pm(r) e^{im\theta} e^{\alpha t}, \quad (35)$$

$$\eta'(\theta, t) = \hat{\eta} e^{im\theta} e^{\alpha t}, \quad (36)$$

where  $\hat{\eta}$  is a constant. We need only consider  $m = 2, 3, 4, \dots$ . Negative  $m$  are redundant for real-valued functions, and  $m = 0$  perturbations aside from the trivial  $a'(t)$  as defined in (16) and governed by (21) would violate incompressibility. Similarly,  $m = 1$  solutions cannot satisfy the  $r \rightarrow \infty$  boundary condition (17) as is usually the case for two-dimensional Stokes flow, most famously for the flow over a circle. It also corresponds to a translation rather than deformation of the membrane and so is irrelevant for the present objectives.

For  $m \geq 2$ , solutions of (9) and (10) require

$$f^\pm(r) = C_1^\pm r^m + C_2^\pm r^{-m} + C_3^\pm r^{2+m} + C_4^\pm r^{2-m}, \quad (37)$$

$$g^\pm(r) = D_1^\pm r^m + D_2^\pm r^{-m}, \quad (38)$$

where all the coefficients are constants to be determined from the boundary conditions. The  $r = 0$  regularity and  $r \rightarrow \infty$  decay conditions indicate

$$C_1^+ = C_3^+ = C_2^- = C_4^- = D_1^+ = D_2^- = 0, \quad (39)$$

so

$$\psi^+(r, \theta, t) = (C_2^+ r^{-m} + C_4^+ r^{2-m}) e^{im\theta} e^{\alpha t}, \quad (40)$$

$$\psi^-(r, \theta, t) = (C_1^- r^m + C_3^- r^{2+m}) e^{im\theta} e^{\alpha t}, \tag{41}$$

$$p^+(r, \theta, t) = D_2^+ r^{-m} e^{im\theta} e^{\alpha t}, \tag{42}$$

$$p^-(r, \theta, t) = D_1^- r^m e^{im\theta} e^{\alpha t}. \tag{43}$$

Since pressure appears directly in the (32) boundary condition, it is useful to have the explicit representation of pressure in (42) and (43), but pressure is not an independent quantity. Substituting (40) through (43) into the governing equation (6) shows that

$$D_1^- = i\mu^- [4m + 4] C_3^- \quad \text{and} \quad D_2^+ = i\mu^+ [4m - 4] C_4^+. \tag{44}$$

Using (44) and substituting the solutions (40) through (36) and (43) into the remaining boundary conditions (18), (22), (32), and (33) yields a linear system for the 5 remaining unknown coefficients,

$$\begin{bmatrix} 2a_o^{m-2}(m-m^2)\lambda & -2a_o^m(m^2+m)\lambda & 2a_o^{-m-2}(m^2+m) & -2a_o^{-m}(m-m^2) & \frac{im\tilde{T}}{a_o^2} - \frac{(im-im^3)\tilde{M}}{a_o^4} \\ ia_o^{m-2}m^2\lambda & ia_o^m(m^2-m-2)\lambda & ia_o^{-m-2}m^2 & ia_o^{-m}(m^2+m-2) & \frac{(m^4-m^2)\tilde{M}}{2a_o^4} - \frac{\tilde{T}}{2a_o^2} + \frac{\tilde{Q}(\lambda-1)}{a_o^3} \\ a_o^m & a_o^{m+2} & -a_o^{-m} & -a_o^{2-m} & 0 \\ a_o^{m-1}m & a_o^{m+1}(m+2) & a_o^{-m-1}m & a_o^{1-m}(m-2) & 0 \\ 0 & 0 & -ia_o^{-m-1}m & -ia_o^{1-m}m & \frac{\tilde{Q}}{2a_o^2} + \alpha \end{bmatrix} \begin{bmatrix} C_1^- \\ C_3^- \\ C_2^+ \\ C_4^+ \\ \hat{\eta} \end{bmatrix} = 0, \tag{45}$$

from which the solvability condition yields an explicit expression for the amplification

$$\alpha = \frac{a_o(\lambda + 1)(2 - 5m\beta - 3m^2)\tilde{Q} + (2m + m^2\beta - m^4\beta - 2m^5)\tilde{M} - a_o^2m^2\beta\tilde{T}}{2a_o^3(\lambda + 1)(3m^2 + m\beta - 2)}, \tag{46}$$

where  $\beta = (\lambda - 1)/(\lambda + 1)$ ,  $\tilde{Q} = Q/\pi$ ,  $\tilde{M} = M/\mu^+$ , and  $\tilde{T} = T/\mu^+$ . Given (36),  $\alpha > 0$  corresponds to linear instability.

### D. Stability results

We focus on cases with  $Q < 0$ , since withdraw is more relevant to the infolding observed for flow into the slit. For  $\lambda \geq 1$  and  $Q > 0$ , (46) shows only damped disturbances ( $\alpha < 0$ ), consistent with the apparent absence of infolding as cells exit the slit.

Figure 11 shows the amplification rate for several sink-flow cases. The simplest case has matched viscosities ( $\lambda = 1$ ) and a passive membrane ( $T = M = 0$ ). In this case, (46) reduces to  $\alpha = -\tilde{Q}/2a_o^2$  and perturbations grow via a simple kinematic mechanism: points on the interface closer to  $r = 0$  simply flow more quickly toward it due to the  $V_r \propto 1/r$  velocity field. This is independent of their wavelength, so all  $m$  modes amplify equally. Increasing the cell interior viscosity for this passive membrane case increases  $\alpha$ , though modestly and only for the longest wavelengths. This behavior reflects a balance of two effects. The dynamic boundary condition provides an amplifying factor that depends upon the viscosity mismatch across the membrane,  $\tilde{Q}(\lambda - 1)/a^3$ , which is seen in the last column of the second row of the matrix in (45) and is a manifestation of the  $Q$ -terms in the normal conditions (32). Though the governing equations are obviously different, this has some similarity to the root mechanism that drives fingering in, for example, Hele-Shaw flow. Fingers form because there is less resistance to pressure in a low-viscosity fluid. However, amplification by this mechanism saturates when the interior viscosity becomes so high that it dominates the dissipation. For large  $\lambda$ , the exterior fluid is relatively inviscid, so the  $(\lambda - 1)$ -dependent driving mechanism is counteracted primarily by the  $\lambda$ -dependent dissipation in the high-viscosity fluid contained within

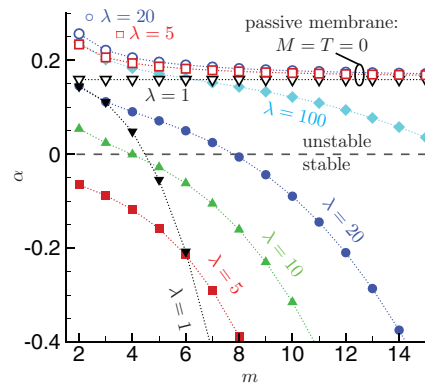


FIG. 11. Mode amplification  $\alpha$  from (46) for  $\tilde{M} = 0.01$ ,  $\tilde{T} = 15$  (solid symbols) and  $\tilde{M} = \tilde{T} = 0$  (open symbols) for  $\nabla$ ,  $\blacktriangledown$   $\lambda = 1$ ;  $\square$ ,  $\blacksquare$   $\lambda = 5$ ;  $\blacktriangle$   $\lambda = 10$ ;  $\circ$ ,  $\bullet$   $\lambda = 20$ ; and  $\blacklozenge$   $\lambda = 100$ . For all cases,  $Q = -1$ . The lines connecting the symbols are to aid in visualization; the spectrum is discrete in  $m$ .

the membrane. As a result, we see only modest increase in amplification between  $\lambda = 5$  and  $\lambda = 20$  in this passive-membrane case. This driving mechanism is also wavelength independent but the increased dissipation due to larger  $\lambda$  acts predominantly at smaller wavelength, disproportionately stabilizing perturbations with larger  $m$ .

For an elastic membrane, we take  $\tilde{M} = 0.01$  and  $\tilde{T} = 15$ . The small  $\tilde{M}$  represents phenomenologically the low bending resistance of the red blood cell membrane, though  $\tilde{M}$  is not analogous to the bending modulus  $E_B$  of Sec. II. In three dimensions, the in-plane shear resistance  $E_S$  also acts to restore the reference shape and is generally more important than  $E_B$  for red blood cells. Thus,  $\tilde{M}$  primarily represents the projected influence of  $E_S$  in two dimensions, though without any formal correspondence. The relatively large  $\tilde{T}$  represents the relatively large resistance to area change ( $E_D$ ) of red blood cell membranes.

It is seen in Figure 11 that these values for  $\tilde{M}$  and  $\tilde{T}$  stabilize all perturbations for  $\lambda = 5$ , but for larger  $\lambda$  the dynamic conditions lead to amplification as the viscosity mismatch overcomes the elastic stabilization for small  $m$ . For  $\lambda = 20$ , several modes have fairly similar growth rates. So, if an initial perturbation is localized on the membrane, it will have a relatively broad spectrum in  $m$ , and we can then expect that it will grow as a relatively localized feature as seen in the infolding. For  $\lambda = 100$ , the membrane elasticity is overwhelmed for small  $m$  and the amplification recovers that for the passive membrane. Indeed for  $\lambda \rightarrow \infty$  in (46) the first term in the numerator dominates the elastic terms and we see a  $\lambda$ - and elasticity-independent behavior for  $\alpha$ . Approaching this limit, the elastic resistance, particularly the bending resistance with its  $m^5$  multiplier, regularizes the instabilities in the short-wavelength ( $m \rightarrow \infty$ ) limit.

Overall, we see a behavior consistent with the infolding of the cells. Noting that  $\beta \rightarrow 1$  for  $\lambda \rightarrow \infty$  and examining the numerator of (46), it can be seen that instability for significant interior viscosity occurs via the same mechanism for either large  $Q$  or large  $\lambda$ . This is consistent with the  $U \propto \lambda^{-1}$  apparent onset of infolding seen in Figure 7, with  $Q/a_o$  here providing the velocity scale. Figure 12 shows the stability boundary in the same fashion as Figure 7 and that it follows  $Q/a_o = U \propto \lambda^{-1}$  for  $\lambda \gtrsim 5$ . For unphysiologically small  $\lambda$ , we see that weaker  $Q < 0$  flows also become unstable. Inspecting the numerator of (46), we see that for  $\lambda \rightarrow 1$ , which corresponds to  $\beta \rightarrow 0$ , the stabilizing  $T$ -term becomes small relative to the destabilizing  $Q$  term. For small  $m$ , bending resistance  $M$  is insufficient to counter this effect, though as expected it stabilizes deformation growth for large  $m$ . This leads to the different shape of the  $\alpha$  curve for  $\lambda = 1$  versus  $\lambda \geq 5$  in Figure 11.

Though  $\lambda \lesssim 5$  is unphysiological for red blood cells, simulations with  $\lambda \leq 1$  also show an infolding, though it is of a different character than for large  $\lambda$ . To illustrate this in the three-dimensional detailed simulations, we consider a modified initial condition that avoids the flow of the cell toward the slit. The cells deform so easily with low  $\lambda$  that cells started in the configuration of Figure 1 become significantly drawn out in the streamwise direction before they reach the slit,

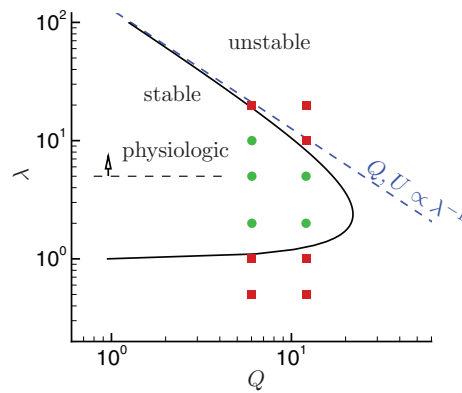


FIG. 12. Stability boundary for  $\tilde{M} = 0.1$ ,  $\tilde{T} = 150$  and  $\bullet$  non-infolding and  $\blacksquare$  infolding simulations (see text and Figure 13). For the cell simulations,  $Q$  is taken to be the mean flow rate per unit length in  $z$  through the slits.

similar to the large  $\vartheta$  cases. Their behavior is therefore more disparate before encountering the slit, so they do not then afford so direct of a comparison between the different cases. To avoid this for assessing  $\lambda < 5$ , all cells were initiated based on a common initial configuration: a  $U = 0.25U_o$  case with  $\lambda = 40$  at the point visualized in Figure 13(a). Starting with this initial condition, the velocity was increased and the viscosity changed to values ranging from  $\lambda = 0.5$  and  $\lambda = 20$ , with the infolding result as indicated in Figure 12 and visualized in Figures 13(b)–13(e). Although there is no expectation of perfect correspondence and  $\tilde{M}$  and  $\tilde{T}$  were adjusted proportionally to establish a fit, the agreement is suggestive. Clearly, infolding can occur for both large and small  $\lambda$ , following the trends anticipated by the instability analysis. The reason for the different infolding character, a blade-like infold in Figure 13(b) versus a cusp-like infold in Figure 13(e), is unclear and probably cannot be fully explained by the present two-dimensional linear analysis. The narrower spectrum of amplified disturbances for small  $\lambda$  (see  $\lambda = 1$  in Figure 11) and the reversed destabilizing role of  $T$  for  $\lambda < 1$  are both candidate possibilities. It is noteworthy that for  $\lambda \leq 1$  cases, the initial dimple seen in Figure 13(a) first decreases before a differently shaped finger amplifies. From a linear-system perspective, this suggests that the unstable eigenvectors underlying the  $\lambda = 40$  infolding configuration used as the initial condition do not provide a good basis for the  $\lambda \leq 1$  infold. However, it might similarly reflect a component of the nonlinear dynamics without analog in the linear model.

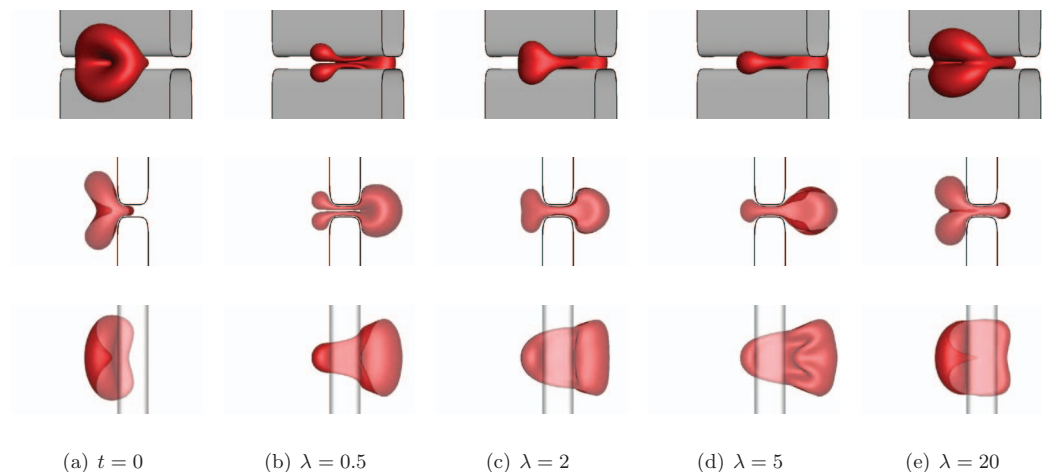


FIG. 13. Visualization of some of the red blood cell cases in Figure 12: (a) The initial condition (see text); (b)–(e) the  $Q = 12.1$  ( $U = 4U_o$ ) cases for the viscosity ratio  $\lambda$  as labeled.

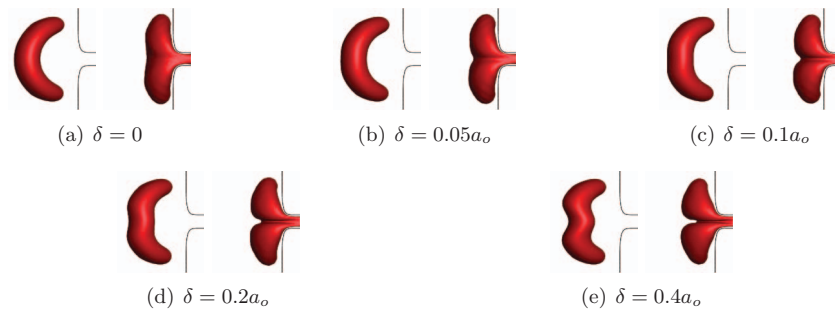


FIG. 14. Perturbed approximately semi-circular initial conditions and shapes  $t = 2.25$  ms later. The perturbation is  $x = \delta \exp[-5y^2/a_0^2]$  with  $\delta$  as labeled (a)–(e) (see Figure 1 for  $x$  and  $y$  definition). The baseline unperturbed  $\delta = 0$  case in (a) was formed by passing a  $\lambda = 1$  cell backward through the slit at a slow  $U = -0.5U_0$ . The flow is then reversed for this study with  $U = 4$  and  $\lambda = 20$ .

It should be noted that none of the amplification rates seen in Figure 11 much exceed the passive-membrane, matched-viscosity amplification  $\alpha = -Q/2\pi a_0$ , which in turn matches the  $\propto Q$  rate of shrinking of the membrane in this model in (21). Thus, we expect that a finite perturbation amplitude is required for it to grow to be significant in the time it takes for the cell to pass the slit. We show in Figure 14 the effect of perturbation amplitude for an approximately semicircular initial cell configuration. Indeed, though they amplify, small perturbations do not lead to complete infolding before the cell passes the slit. Thus, some potentially unstable sets of parameters might avoid infolding if their shape is relatively smooth. This is consistent with the observations of the suppression of infolding with tilt angle and offset shown in Figure 8. The suppressed flow due to the no-slip boundary on the lateral walls of the slit is, however, expected to promote an initial bending of the cell consistent with a finite perturbation that could seed the infolding instability. This is seen, for example, in Figure 5(a): the dimple on the trailing side of the cell becomes more pronounced even before it has a close interaction with the slit.

In Figure 15, we show the short-time growth of an initial perturbation as predicted by (46). The initial perturbation spectrum is taken to be

$$\hat{\eta}_m = a - \frac{a}{20} e^{-m^2/10}, \quad (47)$$

which forms a slightly flattened side of the membrane. This disturbance clearly amplifies as a relatively local feature. A stable case would have a velocity field predominantly in the opposite direction, which would counter the inward flow toward  $r = 0$ , consistent with the behavior seen for the cases discussed in Figure 9. The formation of the very sharp features seen in the infolding

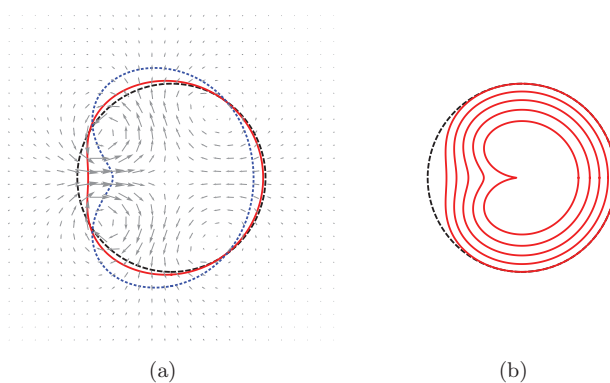


FIG. 15. (a) The growth of an initial perturbation (47) via linear mechanisms overlaying the perturbation velocity field for  $\lambda = 20$ ,  $Q = -1$ ,  $\bar{M} = 0.01$ , and  $\bar{T} = 15$ :  $----$   $r = a_0$ ;  $—$  the initial condition; and  $.....$  at a later time. (b) A solution in the purely kinematic limit (48) with  $\xi_0 = 1 - 0.2e^{-3(\theta-\pi)^2}$ .

simulations are expected to be well beyond what the linear model can represent. However, we close this analysis by noting that the kinematics of the sink flow alone can easily lead to similar sharp features. Consider, for example, the passive advection by (11) of material initially at  $r = \xi(\theta, t)$ , where  $\xi(\theta, t = 0) = \xi_o(\theta)$ . This evolves as

$$\xi(\theta, t) = \sqrt{\xi_o(\theta) + \frac{Q}{2\pi}t}, \quad (48)$$

which is plotted for several times for a specific  $\eta_o$  in Figure 15(b). Algebraic growth into sharp features such as this is thus expected in the kinematic limit, assuming perturbations can initially amplify. In both (45) and (46), we see that the relative effects  $Q$  are stronger for smaller  $a_o$ , which is expected to bring the system closer to this kinematic limit as the cell flows into the slit.

## VI. SUMMARY AND CONCLUSIONS

Three distinct behaviors were observed for the flow of red blood cells through a small slit, a model for small slit-like passages in the spleen. For slow flow, as anticipated, cells become trapped, with the flow insufficient to overcome their elastic resistance to the deformations necessary for them to fully fit into the slit. Cells trapped in this way would presumably be more easily found and engulfed by the macrophages that are thought to ultimately remove them from circulation. However, the trapping is independent of the interior viscosity, which is known to increase during the cell lifetime. Thus, it is unclear how senescent cells would be distinguished. Limited data suggest that cells trapped in this way do, over the course of many seconds to minutes, pass the slit, which might occur via longer-time-scale cytoskeletal remodeling. Aging might also diminish their capacity to remodel.

As expected, when the flow is strong enough, the cells do deform and pass through the slit. Their geometry as they pass is similar to that seen in micrographs of fixed sections of the spleen.<sup>9,11</sup> In these cases, the cells are slowed significantly, and pass the slit at well less than the average speed of the plasma, which would augment the concentration of cells in upstream red pulp region of the spleen. Those with a cytosol viscosity elevated as expected for older cells pass significantly more slowly.

For larger elastic capillary numbers, a peculiar infolding occurs. This is phenomenologically similar to that suggested by a linear stability analysis of a model system, where the slit flow is modeled by a simple sink flow. The implications of the infolding for actual red blood cells, however, is difficult to anticipate, especially given that the sharp features that develop are beyond the range of accuracy expected for the relatively simple constitutive model employed. Though the onset of this behavior is mesh independent, it would seem that a significantly denser mesh would be required to resolve them in detail. It is possible that a so-folded cell might be significantly slowed or even trapped. Since infolding occurs with greater likelihood for the higher cytosol capillary numbers, which is expected to be a key mechanical characteristic of senescent red blood cells, this would be consistent with their removal. It is also possible that the severe deformations associated with the infolding might promote degradation of the cells or even lead to lysis.

The linear stability analysis anticipated, and detailed simulations confirmed, that unphysiologically low cytosol viscosity also exposes the cells to an infolding instability. This is not probably important for flow in the spleen, but it does have the interesting implication that the physiologic  $\lambda \approx 5$  cytosol viscosity is protective against this class of severe deformations.

Because it is not possible to faithfully represent even with our detailed flow model all the complexity of any such biological system, our conclusions in regards to the spleen *per se* must remain somewhat speculative until more observations are available. Regardless, these types of behaviors will potentially be important in the design of devices that handle blood on a cell-by-cell basis. They might, for example, serve as a mechanical mechanism for sorting cells based upon their interior viscosity.

## ACKNOWLEDGMENTS

This work was presented at the Directions in Computational Flow Physics workshop honoring Professor Parviz Moin upon his 60th birthday and recognizing his vast contributions to this field. I was first shown the potential of computational flow physics by Professor Moin and remain indebted to him for continued inspiration and sound advice. Support from National Science Foundation (NSF) (CBET 09-32607) is gratefully acknowledged.

- <sup>1</sup> S. Guido and G. Tomaiuolo, "Microconfined flow behavior of red blood cells *in vitro*," *C. R. Phys.* **10**, 751 (2009).
- <sup>2</sup> A. R. Pries, T. W. Secomb, and P. Gaechgens, "Biophysical aspects of blood flow in the microvasculature," *Cardiovasc. Res.* **32**, 654 (1996).
- <sup>3</sup> A. S. Popel and P. C. Johnson, "Microcirculation and hemorheology," *Annu. Rev. Fluid Mech.* **37**, 43 (2005).
- <sup>4</sup> S. Suresh, "Mechanical response of human red blood cells in health and disease: Some structure-property-function relationships," *J. Mater. Res.* **21**, 1871 (2006).
- <sup>5</sup> M. Toner and D. Irimia, "Blood-on-a-chip," *Annu. Rev. Biomed. Eng.* **7**, 77 (2005).
- <sup>6</sup> G. Deplaine, I. Safeukui, F. Jeddi, F. Lacoste, V. Brousse, S. Perrot, S. Biligui, M. Guillotte, C. Guitton, S. Dokmak, B. Aussilhou, A. Sauvanet, D. C. Hatem, F. Paye, M. Thellier, D. Mazier, G. Milon, N. Mohandas, O. Mercereau-Puijalon, P. H. David, and P. A. Buffet, "The sensing of poorly deformable red blood cells by the human spleen can be mimicked *in vitro*," *Blood* **117**, e88 (2011).
- <sup>7</sup> R. E. Mebius and G. Kraal, "Structure and function of the spleen," *Nat. Rev. Immun.* **5**, 606 (2005).
- <sup>8</sup> L.-T. Chen and L. Weiss, "The role of the sinus wall in the passage of erythrocytes through the spleen," *Blood* **41**, 529 (1973).
- <sup>9</sup> L. Weiss, "A scanning electron microscopic study of the spleen," *Blood* **43**, 665 (1974).
- <sup>10</sup> H. A. del Portillo, M. Ferrer, T. Brugat, L. Martin-Jaular, J. Langhorne, and M. V. G. Lacerda, "The role of the spleen in malaria," *Cell. Microbiol.* **14**, 343 (2012).
- <sup>11</sup> A. C. Groom, E. E. Schmidt, and I. C. MacDonald, "Microcirculatory pathways and blood flow in spleen: New insights from washout kinetics, corrosion casts, and quantitative intravital videomicroscopy," *Scanning Microsc.* **5**, 159 (1991).
- <sup>12</sup> C. L. Witte, M. H. Witte, G. C. McNeill, J. N. Hall, G. P. Van der Werf, and J. M. Woolfenden, "Splenic salvage quantified by uptake of heat-damaged radiolabeled red blood cells," *Am. J. Surg.* **155**, 303 (1988).
- <sup>13</sup> Y. Sugawara, Y. Hayashi, Y. Shigemasa, Y. Abe, I. Ohgushi, E. Ueno, and F. Shimamoto, "Molecular biosensing mechanisms in the spleen for the removal of aged and damaged red cells from the blood circulation," *Sensors* **10**, 7099 (2010).
- <sup>14</sup> B. Schnitzer, T. M. Sodeman, M. L. Mead, and P. G. Contacos, "An ultrastructural study of the red pulp of the spleen in malaria," *Blood* **41**, 207 (1973).
- <sup>15</sup> S. Suresh, J. Spatz, J. P. Mills, A. Micoulet, M. Dao, C. T. Lim, M. Beil, and T. Seufferlein, "Connections between single-cell biomechanics and human disease states: Gastrointestinal cancer and malaria," *Acta Biomater.* **1**, 15 (2005).
- <sup>16</sup> R. I. Weed, "The importance of erythrocyte deformability," *Am. J. Med.* **49**, 147 (1970).
- <sup>17</sup> D. Shemin and D. Rittenberg, "The life span of the human red blood cell," *J. Biol. Chem.* **116**, 627 (1946).
- <sup>18</sup> M. R. Clark, "Senescence of red blood cells: Progress and problems," *Physiol. Rev.* **68**, 503 (1988).
- <sup>19</sup> M. Costa, I. Ghiran, C.-K. Peng, A. Nicholson-Weller, and A. L. Goldberger, "Complex dynamics of human red blood cell flickering: Alterations with *in vivo* aging," *Phys. Rev. E* **78**, 020901(R) (2008).
- <sup>20</sup> Y. K. Park, C. A. Best, K. Badizadegana, R. R. Dasaria, M. S. Feld, T. Kuriabovad, M. L. Henlee, A. J. Levine, and G. Popescua, "Measurement of red blood cell mechanics during morphological changes," *Proc. Natl. Acad. Sci. U.S.A.* **107**, 6731 (2010).
- <sup>21</sup> T. Shiga, M. Sekiya, N. Maeda, K. Kon, and M. Okazaki, "Cell age-dependent changes in deformability and calcium accumulation of human erythrocytes," *Biochim. Biophys. Acta* **814**, 289 (1985).
- <sup>22</sup> C. Pfafferoth, G. B. Nash, and H. J. Meiselman, "Red blood cell deformation in shear flow: Effects of internal and external phase viscosity and of *in vivo* aging," *Biophys. J.* **47**, 695 (1985).
- <sup>23</sup> F. H. Bosch, J. M. Werre, L. Schipper, B. Roerdinkholder-Stoelwinder, T. Huls, F. L. A. Willekens, G. Wichers, and M. R. Halie, "Determinants of red blood cell deformability in relation to cell age," *Eur. J. Haematol.* **52**, 35 (1994).
- <sup>24</sup> G. R. Cokelet and H. J. Meiselman, "Rheological comparison of hemoglobin solutions and erythrocyte suspensions," *Science* **162**, 275 (1968).
- <sup>25</sup> M. Iino and Y. Okuda, "Concentration dependence of Brownian motion and the viscosity of hemoglobin solutions," *Jpn. J. Appl. Phys.* **36**, 3786 (1997).
- <sup>26</sup> A. R. Williams and D. R. Morris, "The internal viscosity of the human erythrocyte may determine its lifespan *in vivo*," *Scand. J. Haematol.* **24**, 57 (1980).
- <sup>27</sup> E. T. A. Mohamed, A. E. Kamanyi, M. Pluta, and W. Grill, "Age-dependent acoustic and microelastic properties of red blood cells determined by vector contrast acoustic microscopy," *Microsc. Microanal.* **18**, 436 (2012).
- <sup>28</sup> O. Linderkamp and H. J. Meiselman, "Geometric, osmotic, and membrane mechanical properties of density-separated human red cells," *Blood* **59**, 1121 (1982).
- <sup>29</sup> P. J. H. Bronkhorst, G. J. Streekstra, J. Grimbergen, E. J. Nijhof, J. J. Sixma, and G. J. Brakenhoff, "A new method to study shape recovery of red blood cells using multiple optical trapping," *Biophys. J.* **69**, 1666 (1995).
- <sup>30</sup> G. B. Nash and H. J. Meiselman, "Red cell and ghost viscoelasticity: Effects of hemoglobin concentration and *in vivo* aging," *Biophys. J.* **43**, 63 (1983).
- <sup>31</sup> S. Weinbaum, J. M. Tarbell, and E. R. Damiano, "The structure and function of the endothelial glycocalyx layer," *Annu. Rev. Biomed. Eng.* **9**, 121 (2007).

- <sup>32</sup>R. Skalak, A. Tozeren, R. P. Zarda, and S. Chien, "Strain energy function of red blood-cell membranes," *Biophys. J.* **13**, 245 (1973).
- <sup>33</sup>C. Pozrikidis, "Axisymmetric motion of a file of red blood cells through capillaries," *Phys. Fluids* **17**, 031503 (2005).
- <sup>34</sup>H. Zhao, A. H. G. Isfahani, L. Olson, and J. B. Freund, "A spectral boundary integral method for flowing blood cells," *J. Comput. Phys.* **229**, 3726 (2010).
- <sup>35</sup>J. B. Freund and H. Zhao, "A fast high-resolution boundary integral method for multiple interacting blood cells," in *Computational Hydrodynamics of Capsules and Biological Cells*, edited by C. Pozrikidis (Chapman & Hall, Boca Raton, FL, 2010), pp. 71–111.
- <sup>36</sup>S. Kim and S. J. Karrila, *Microhydrodynamics: Principles and Selected Applications* (Butterworth-Heinemann, Boston, 1991).
- <sup>37</sup>C. Pozrikidis, *Boundary Integral and Singularity Methods for Linearized Viscous Flow* (Cambridge University Press, Cambridge, 1992).
- <sup>38</sup>J. B. Freund and M. M. Orescanin, "Cellular flow in a small blood vessel," *J. Fluid Mech.* **671**, 466 (2011).
- <sup>39</sup>J. B. Freund and B. Shapiro, "Transport of particles by magnetic forces and cellular blood flow in a model microvessel," *Phys. Fluids* **24**, 051904 (2012).
- <sup>40</sup>J. Li, G. Lykotrafitis, M. Dao, and S. Suresh, "Cytoskeletal dynamics of human erythrocyte," *Proc. Natl. Acad. Sci. U.S.A.* **104**, 4937 (2007).